The Astrophysical Journal, 981:57 (13pp), 2025 March 1 https://doi.org/10.3847/1538-4357/adafa1

New Perspective on the Multiple-population Phenomenon in Galactic Globular Clusters from a Wide-field Photometric Survey

S. Jang[1], A. P. Milone[2,3], A. F. Marino[3,4], M. Tailo[3], E. Dondoglio[2], M. V. Legnardi[2], G. Cordoni[5], T. Ziliotto[2], E. P. Lagioia[6], M. Carlos[7], A. Mohandasan[2], E. Bortolan[2], and Y.-W. Lee[1]
[1] Center for Galaxy Evolution Research and Department of Astronomy, Yonsei University, Seoul 03722, Republic of Korea
[2] Dipartimento di Fisica e Astronomia "Galileo Galilei," Università di Padova, Vicolo dell'Osservatorio 3, I-35122, Padua, Italy
[3] Istituto Nazionale di Astrofisica—Osservatorio Astronomico di Padova, Vicolo dell'Osservatorio 5, IT-35122, Padua, Italy
[4] Istituto Nazionale di Astrofisica—Osservatorio Astrofisico di Arcetri, Largo Enrico Fermi, 5, Firenze 50125, Italy
[5] Research School of Astronomy and Astrophysics, Australian National University, Canberra, ACT 2611, Australia
[6] South-Western Institute for Astronomy Research, Yunnan University, Kunming 650500, People's Republic of China
[7] Department of Physics and Astronomy, Uppsala University, Box 516, SE-751 20 Uppsala, Sweden
Received 2024 November 13; revised 2025 January 17; accepted 2025 January 27; published 2025 February 26

Abstract

Wide-field photometry of Galactic globular clusters (GCs) has been investigated to overcome limitations from the small field of view of the Hubble Space Telescope in the study of multiple populations. In particular, "chromosome maps" (ChMs) built with ground-based photometry were constructed to identify the first- and second-generation (1G and 2G) stars over the wide field of view. The ChMs allow us to derive the fraction of distinct populations in an analyzed field of view. We present here the radial distribution of the 2G fraction in 29 GCs. The distributions show that all the GCs have either a flat distribution or more centrally concentrated 2G stars. Notably, we find that the fraction of 1G stars outside the half-light radius is clearly bifurcated across all mass range. It implies that a group of GCs with lower 1G fractions (hereafter Group II) have efficiently lost their 1G stars in the outermost cluster regions. In fact, in connection with the trends of the radial distribution, most GCs of Group II have spatially mixed populations, while only less massive GCs in Group I (a group with higher 1G fraction) show that feature. Lastly, we investigate links between these two groups and host cluster parameters. We find that most GCs of Group II are distributed along a broader range of galactocentric distances with smaller perigalactic distances < 3.5 kpc. Besides, by using the Gaia data, it is observed that Group II GCs have higher energy on the integrals of motion diagrams than Group I GCs.

Unified Astronomy Thesaurus concepts: Globular star clusters (656); Population II stars (1284); Photometry (1234)

1. Introduction

Observational evidence demonstrated that nearly all Galactic globular clusters (GCs) contain two main groups of stellar populations: a first population (hereafter 1G) with chemical composition similar to halo field stars, and a second population (2G) enriched in helium, nitrogen, and sodium and depleted in carbon and oxygen (see Y. W. Lee et al. 1999; R. Gratton et al. 2004; Y.-W. Lee et al. 2005; A. F. Marino et al. 2008; E. Carretta et al. 2009; A. Renzini et al. 2015; A. P. Milone et al. 2017, 2020, and references therein). In the past two decades, the multiple populations in GCs have been widely investigated, but the formation history to explain the observed abundance anomalies is a matter of ongoing debate (see N. Bastian et al. 2018; R. Gratton et al. 2019; A. P. Milone & A. F. Marino 2022, for recent reviews).

Some scenarios on the formation of multiple stellar populations assume that multiple populations are attributed to distinct bursts of star formation at different epochs, with 2G stars born from materials processed and ejected by 1G stars (e.g., T. Decressin et al. 2007; S. E. de Mink et al. 2009; P. A. Denissenkov & F. D. A. Hartwick 2014; S. Jang et al. 2014; S. Jang & Y.-W. Lee 2015; Y.-W. Lee et al. 2015; F. D'Antona et al. 2016; Y.-W. Lee & S. Jang 2016; J. J. Kim & Y.-W. Lee 2018; A. Renzini et al. 2022). One problem of these scenarios is that the enriched stars are predicted to only constitute a very small fraction of the total initial mass of clusters. Observations, however, have shown that the number fractions of 1G and 2G stars are quite similar in most GCs (e.g., E. Carretta et al. 2009; A. P. Milone et al. 2017), which is referred to as the "mass budget problem." To address the problem, it is necessary for 1G stars to have been considerably more massive at their formation and subsequently lost a large fraction of 1G stars (>90%), thereby making a significant contribution to the assembly of the Galactic halo (A. D'Ercole et al. 2008; C. Conroy 2012; A. Renzini et al. 2015). Alternative scenarios propose that all GC stars are coeval and that chemical enrichment of 2G stars is attributed to accretion of materials processed by massive or supermassive stars onto pre-main-sequence stars (e.g., N. Bastian et al. 2013; M. Gieles et al. 2018). It is also suggested that stellar mergers might be responsible for multiple populations in GCs (L. Wang et al. 2020).

Most of the multigeneration scenarios predict that 2G stars would form a more centrally segregated stellar subsystem than spatially extended 1G stars (e.g., A. D'Ercole et al. 2008; P. A. Denissenkov & F. D. A. Hartwick 2014; A. Renzini et al. 2015; F. D'Antona et al. 2016; M. Gieles et al. 2018, and references therein). Over time, long-term dynamic evolution gradually diminishes the initial structural differences between 1G and 2G stars, although the strength and the progress of the evolution vary from one cluster to another. Indeed, some GCs are expected to retain memory of their initial distribution, while some can host spatially fully mixed 1G and 2G stars

(e.g., E. Vesperini et al. 2013; E. Dalessandro et al. 2019; E. Leitinger et al. 2023). E. Dalessandro et al. (2019) used Hubble Space Telescope (HST) photometry to investigate the radial distribution of 1G and 2G stars as a function of the age/relaxation time referred to as "dynamical age." They discovered that clusters with young dynamical ages preferentially have more centrally concentrated 2G stars, lending more support to the multigeneration scenarios.

Numerous photometric studies on multiple populations have demonstrated that this phenomenon is most efficiently identified with appropriate combinations of ultraviolet, optical, and near-infrared bands of HST and the James Webb Space Telescope (JWST; e.g., A. P. Milone et al. 2012a, 2020, 2023a, 2023b; G. Piotto et al. 2015; F. Niederhofer et al. 2017; E. P. Lagioia et al. 2019, 2025; E. Dondoglio et al. 2021, 2023; S. Jang et al. 2021; G. Cordoni et al. 2022, 2023; M. V. Legnardi et al. 2022, 2023; A. F. Marino et al. 2024; A. Mohandasan et al. 2024). In particular, the pseudo–two-color diagram dubbed the "chromosome map" (ChM) of red giant branch (RGB) stars based on the HST photometry is well-known as one of the most effective photometric tools to disentangle multiple stellar populations in GCs. The ChMs of 57 GCs constructed by A. P. Milone et al. (2017), which were built with a combination of stellar magnitudes in the F275W, F336W, F438W, and F814W filters of HST, allowed for a homogeneous and extensive analysis of the multiple-population phenomenon with unprecedented detail.

One of the main limitations of the HST camera is its small field of view, which restricts studies on GCs and their stellar populations to the innermost cluster region. To extend the investigation to the entire cluster, it is mandatory to use wide-field photometry by means of photometric diagrams sensitive to the chemical composition of distinct stellar populations, such as photometry from suitable narrowband filters (J.-W. Lee 2017), color–magnitude diagrams (CMDs), and pseudo-CMDs built with Strömgren photometry (e.g., F. Grundahl et al. 1998; D. Yong & F. Grundahl 2008) or appropriate combinations of the U, B, V and I Johnson–Cousins bands (e.g., A. F. Marino et al. 2008; A. P. Milone et al. 2010, 2012b; M. Monelli et al. 2013; E. Dondoglio et al. 2021; E. Leitinger et al. 2023). S. Jang et al. (2022) exploited photometric diagrams of $C_{U,B,I} = (U - B) - (B - I)$ pseudocolor and $B - I$ color, which are sensitive to stellar populations with different light-element and helium abundances along RGB stars (M. Monelli et al. 2013; G. Cordoni et al. 2020), to introduce ChMs from the wide-field ground-based photometry. They showed potentials of these ChMs by deriving the radial distribution of stellar populations in NGC 288 and the fraction of 1G stars in the field of view of the ground-based photometry for NGC 1904, NGC 4147, NGC 6712, NGC 7006, and NGC 7492.

In this paper, we extend the analysis of S. Jang et al. (2022) to the ChMs of 29 GCs to extensively investigate the multiple-population phenomenon over a wide field of view. The paper is organized as follows: The data and data analysis are described in Section 2, while Section 3 presents the radial distribution of the fraction of 2G stars in 29 GCs. In Section 4, we derive the fraction of 1G stars in the analyzed field of view and in the region inside and outside the half-light radius from the ChMs of 29 GCs. Furthermore, we examine possible links between the properties we found and the GC global parameters to investigate the dependence of the multiple-population phenomenon on the galactic environment. To do this, we use kinematic data and the probable merging events for Galactic GCs provided by Gaia Collaboration et al. (2018) and D. Massari et al. (2019). Summary and conclusions are provided in Section 5.

2. Data Analysis

To investigate the multiple-population phenomenon over a wide field of view, we have exploited the $\Delta c_{U,B,I}$ versus $\Delta_{B,I}$ pseudo–two-color diagrams of RGB stars for 29 GCs from S. Jang et al. (2022). In their work, they analyzed the state-of-art photometry and astrometry of 43 GCs provided by P. B. Stetson et al. (2019) for 43 Galactic GCs. For each cluster, they identified probable cluster members by combining photometry with stellar proper motions and parallax measurements from Gaia eDR3 (Gaia Collaboration et al. 2021). Additionally, they derived high-resolution reddening maps and corrected the photometry for differential reddening if necessary. The $\Delta c_{U,B,I}$ versus $\Delta_{B,I}$ ChMs were derived from the I versus $C_{U,B,I}$ pseudo-CMD and the I versus $B - I$ CMD, which maximize the separation between distinct stellar populations. For more information about the ChMs of 29 Galactic GCs, the reader may refer to S. Jang et al. (2022).

Although the ground-based catalogs cover almost the whole area of each cluster, higher stellar density in the central region causes blending to affect the photometry of stars. Thus, a number of stars located in the central region are removed in the step taken to select a sample of well-measured stars before separating stellar populations. Indeed, 96% and 81% of the analyzed stars in 29 GCs are located outside their core and half-light radii, respectively, which implies that the results from this study are more representative of the region outside of the central region of clusters. In this context, we found a strong correlation between the median radius of the analyzed stars, $R_{\rm median}$, and the tidal radius of clusters taken from the 2010 version of the W. E. Harris (1996) catalog, $r_{\rm tidal}$, as shown in the left panel of Figure 1. This is confirmed by the Spearman's rank correlation coefficient, $R_{\rm S} = 0.86$, which is significant at p-value < 0.00001. Thus, the cluster mass correlates with $\log(R_{\rm median}/r_{\rm core})$ as shown in the right panel, which is expected from the well-known relation between the cluster mass and the King-model central concentration defined as $\log(r_{\rm tidal}/r_{\rm core})$. The uncertainty associated with $R_{\rm median}$ is calculated by bootstrapping with replacement over the sample of RGB stars and then repeated 1000 times. We adopted this method owing to its suitability for data with small sample sizes or unknown distributions. We considered one standard deviation of the bootstrapped measurements as an error estimate.

Figure 2 illustrates the procedure to derive the fraction of 1G stars in NGC 2808 from its ChM. We mostly followed the method by A. P. Milone et al. (2017, see their Figure 8), which was applied on the $\Delta c_{\rm F275W,F336W,F814W}$ versus $\Delta_{\rm F275W,F814W}$ diagram. S. Jang et al. (2022) noticed that the slope of the 1G stars in the ground-based ChMs of GCs with extended 1G sequences seems to vary from cluster to cluster, which has not been observed in the ChMs based on HST photometry. For obtaining a new coordinate system where 1G and 2G stars could be easily identified, we defined by eye a gap between 1G and 2G stars with a line (see the dashed red line in the top left panel). We then took as 1G stars those below the red line, while we defined the remaining stars as 2G stars in all the panels, which are colored blue and black, respectively. The red ellipse

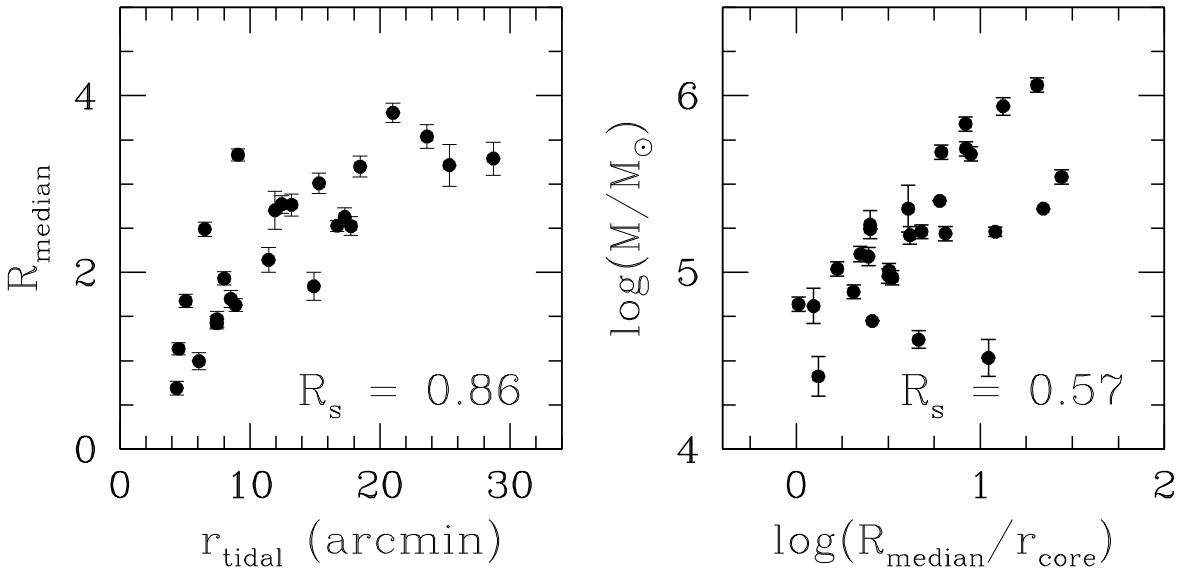

Figure 1. $R_{\rm median}$ against the tidal radius of the cluster (from the 2010 version of the W. E. Harris 1996 catalog). The Spearman's rank correlation coefficients ($R_{\rm S}$) are reported in each panel.

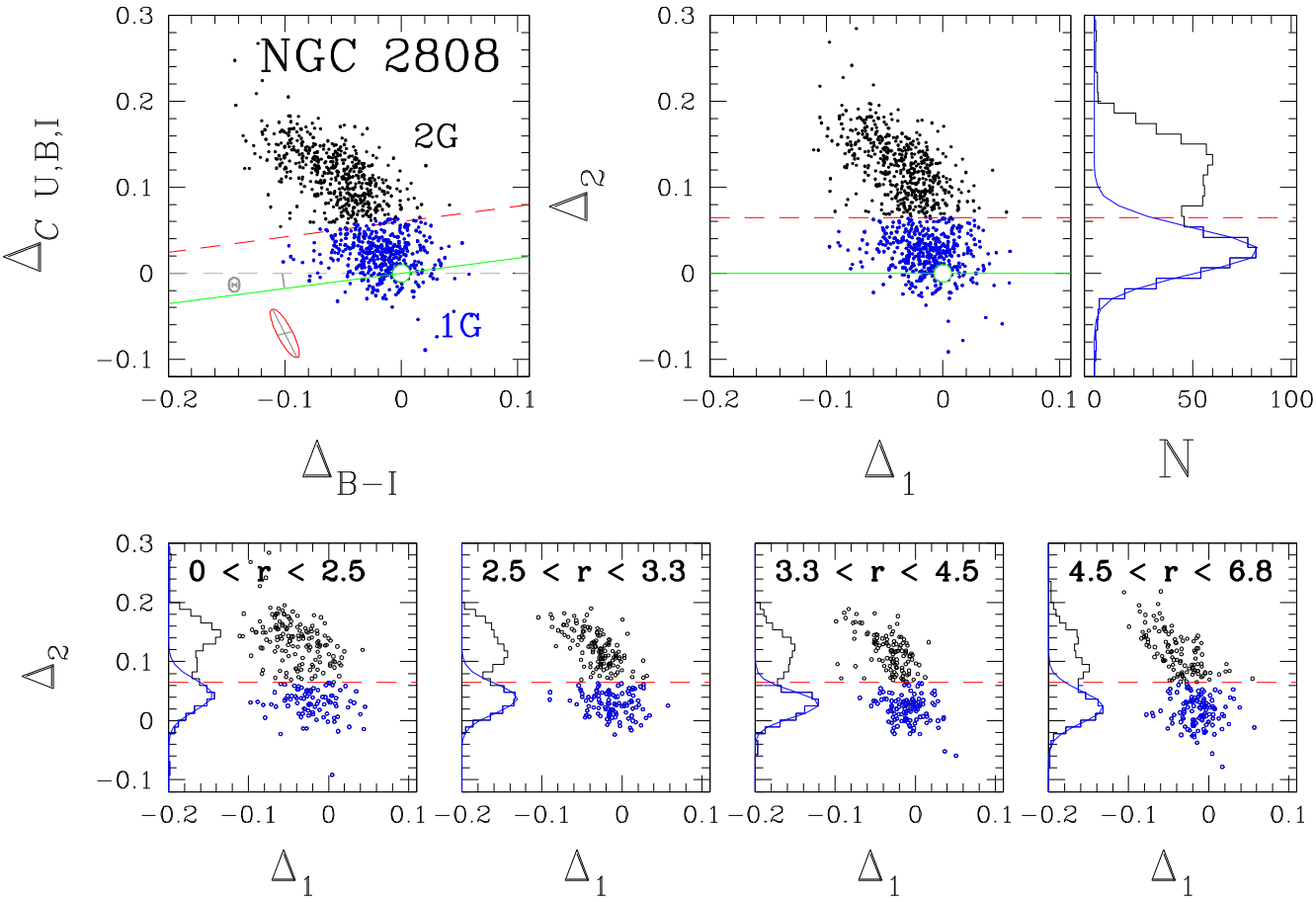

Figure 2. Top panels: the procedure used to identify 1G and 2G stars in NGC 2808 and derive the number fraction of each population. The top left panel shows the wide-field ground-based ChM $\Delta c_{U,B,I}$ vs. $\Delta_{B,I}$ in NGC 2808, which is adopted from S. Jang et al. (2022). The red dashed line drawn by eye separates the selected 1G and 2G stars, which are colored blue and black, respectively. The green line has the same angle Θ as the red dashed line with respect to the horizontal line but goes through the frame's origin. The new coordinates Δ_2 vs. Δ_1 in the top middle panel are reproduced by rotating clockwise by the angle Θ the plot in the top left panel. The histogram in the top right panel shows the distributions of the Δ_2 values. The red ellipse in the top left panel shows the distribution of the observational error. Bottom panels: same as the top middle and right panels, but at different radial intervals from the cluster center.

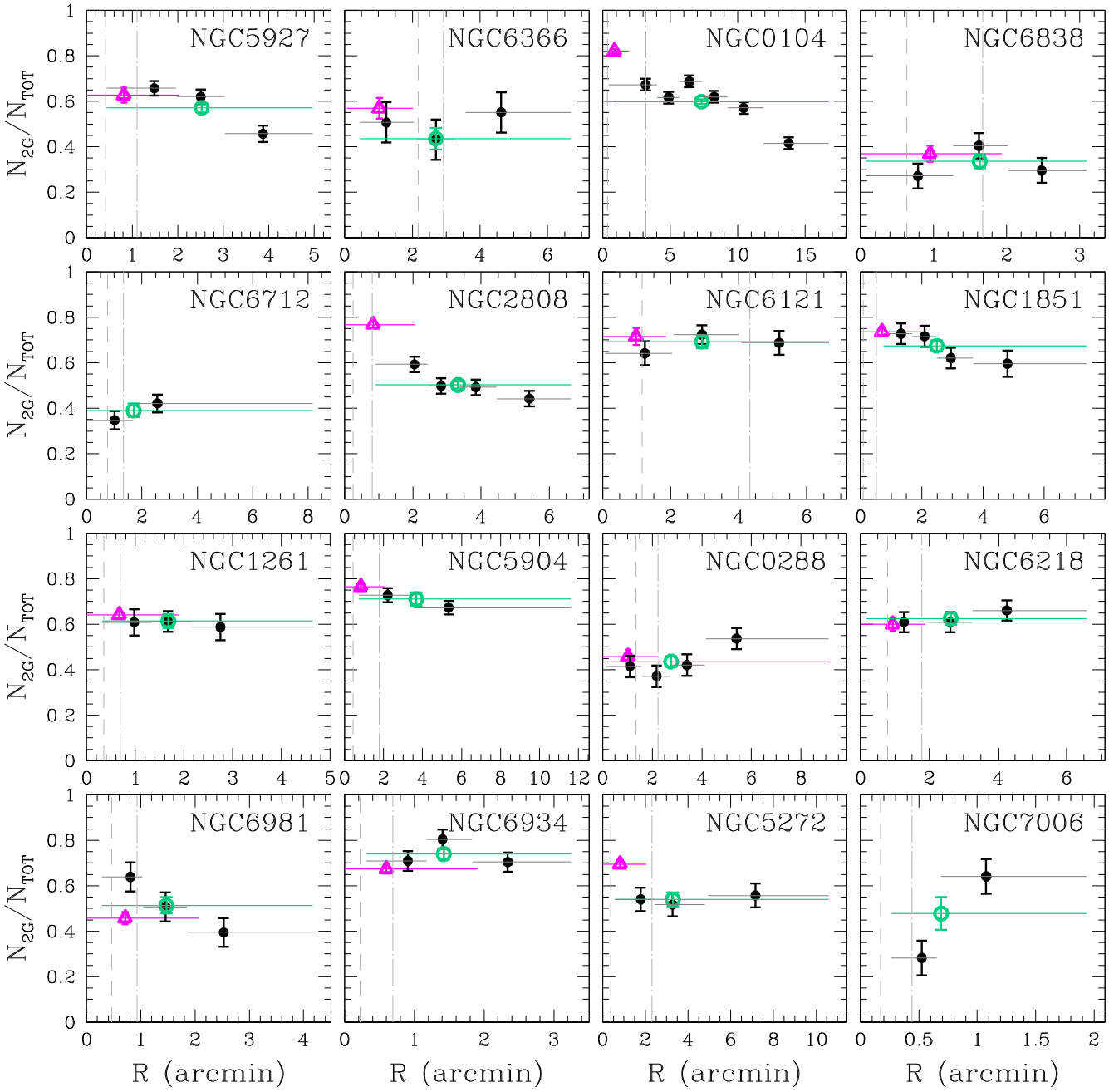

Figure 3. Fraction of 2G stars as a function of radial distance for NGC 5927, NGC 6366, NGC 104, NGC 6838, NGC 6712, NGC 2808, NGC 6121, NGC 1851, NGC 1261, NGC 5904, NGC 288, NGC 6218, NGC 6981, NGC 6934, NGC 5272, and NGC 7006. The clusters are sorted according to their metallicity, from the most metal-rich to the most metal-poor. Black circles mark the results derived from ground-based ChMs of GCs, whereas the aqua circle indicates the 2G fraction in the analyzed entire field of view. The magenta triangle indicates the fraction of 2G stars from A. P. Milone et al. (2017, 2020) based on the HST photometry. Horizontal lines mark the extension of each radial interval. The vertical dashed and dashed–dotted lines indicate the core and the half-light radius, respectively.

shown in the top left panel indicates the expected distributions of the observational errors and includes 68.27% of the simulated stars. The green line has the same angle Θ as the dashed red line, with respect to the horizontal line, but it goes through the origin of the frame. The new coordinate Δ_2 versus Δ_1 in the top middle panel is generated by rotating the top left panel diagram by the angle Θ around the origin of the reference frame. The histogram plotted in the top right panel represents the Δ_2 distribution of stars in the cluster. To estimate the fraction of 1G stars with respect to the total number of stars, the Gaussian function is fitted to the histogram distribution of the selected 1G stars (blue solid line in the top right panel of Figure 2), and we derive the fraction as the ratio between the area under the Gaussian and the total number of stars in the ChM. The bottom panels of Figure 2 illustrate the same procedure described above, but performed with the groups of stars at different radial intervals from the cluster center to derive the radial distribution of the 1G fraction. The radial intervals indicated in the bottom panels are determined to include the same number of stars in each interval. The resulting radial distribution of the fraction of 2G stars in NGC 2808 is illustrated in one panel of Figure 3.

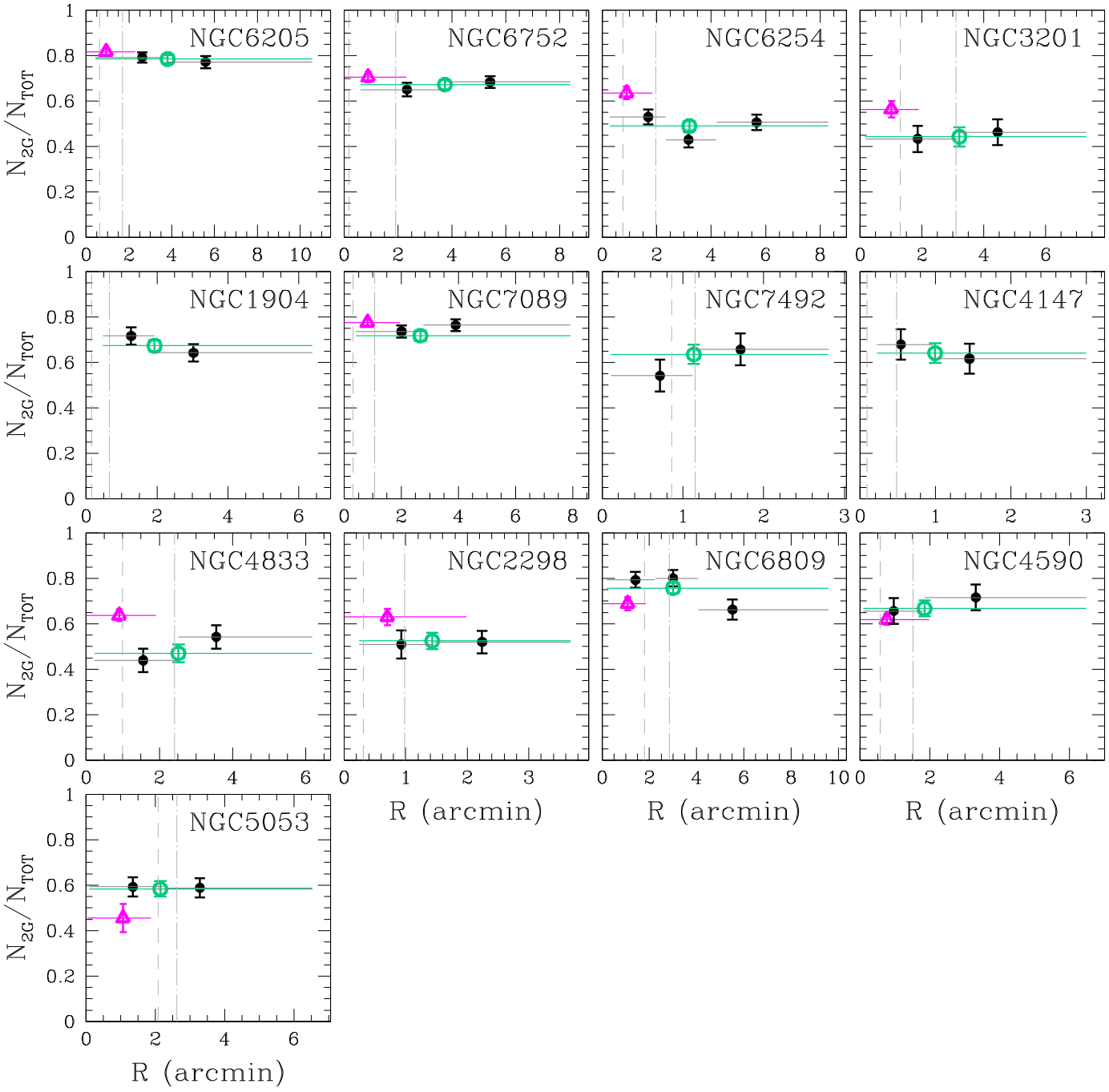

Figure 4. Same as Figure 3, but for NGC 6205, NGC 6752, NGC 6252, NGC 3201, NGC 1904, NGC 7089, NGC 7492, NGC 4147, NGC 4833, NGC 2298, NGC 6809, NGC 4590, and NGC 5053.

As described above, the analyses presented in this paper are mostly limited to stars in the outermost cluster regions. Numerous studies have found that there are differences in internal dynamics and radial distributions between 1G and 2G stars in many clusters (e.g., M. Libralato et al. 2023; G. Cordoni et al. 2025). Therefore, the criteria for our selection pose limitations in interpreting the results and understanding the properties of the entire cluster. In that regard, using the HST data for the inner cluster region in combination with the ground-based data provides a significant advantage in performing a homogeneous analysis of the wide-field spatial extent of a large sample of GCs (e.g., E. Leitinger et al. 2023). A. P. Milone et al. (2017) documented the fractions of 1G stars in Galactic GCs, which were derived from the HST-based ChMs of RGB stars. In this paper, we used these 1G fractions by A. P. Milone et al. (2017) for the inner cluster region, together with our results, to investigate multiple populations over a wide field of view. We note that stars excluded during our photometric cleaning, along with cluster regions without observed stars caused by the limitations of the field of view for some clusters, might introduce uncertainties in the number density profile as a function of radius, potentially leading to subtle biases in our results.

3. Radial Distribution of the Fraction of 2G Stars in 29 GCs

Figures 3 and 4 illustrate a collection of the radial distribution of the number fraction of 2G stars in 29 GCs as

Table 1
The Fraction of 1G Stars Measured in Different Regions of the Cluster

ID	N_{1G}/N_{TOT}	N_{stars}	R_{median}/r_{hl}	N_{1G}/N_{TOT} ($>r_{hl}$)[a]	N_{stars} ($>r_{hl}$)	N_{1G}/N_{TOT} ($<r_{hl}$)[b]	Group
NGC 104	0.40 ± 0.01	2095	2.31	0.40 ± 0.01	1923	0.18 ± 0.01	1
NGC 288	0.56 ± 0.02	430	1.24	0.55 ± 0.03	266	0.54 ± 0.03	1
NGC 1261	0.39 ± 0.03	264	2.47	0.38 ± 0.03	251	0.35 ± 0.03	2
NGC 1851	0.33 ± 0.03	353	4.88	0.33 ± 0.03	353	0.26 ± 0.03	2
NGC 1904	0.33 ± 0.03	319	2.97	0.33 ± 0.03	313	⋯	2
NGC 2298	0.48 ± 0.04	164	1.46	0.44 ± 0.04	116	0.41 ± 0.07	2
NGC 2808	0.50 ± 0.02	942	4.16	0.50 ± 0.02	942	0.22 ± 0.02	1
NGC 3201	0.56 ± 0.04	143	1.04	0.50 ± 0.05	75	0.44 ± 0.04	1
NGC 4147	0.36 ± 0.04	92	2.08	0.36 ± 0.05	78	⋯	2
NGC 4590	0.33 ± 0.04	143	1.22	0.26 ± 0.05	87	0.39 ± 0.04	2
NGC 4833	0.53 ± 0.04	194	1.05	0.45 ± 0.05	102	0.36 ± 0.03	1
NGC 5053	0.42 ± 0.03	236	0.82	0.40 ± 0.05	95	0.54 ± 0.06	2
NGC 5272	0.46 ± 0.03	292	1.42	0.46 ± 0.03	202	0.31 ± 0.01	1
NGC 5904	0.29 ± 0.03	396	2.08	0.26 ± 0.03	345	0.24 ± 0.02	2
NGC 5927	0.43 ± 0.02	662	2.30	0.43 ± 0.02	625	0.38 ± 0.04	1
NGC 6121	0.31 ± 0.03	289	0.68	0.30 ± 0.05	81	0.29 ± 0.04	2
NGC 6205	0.21 ± 0.02	526	2.25	0.21 ± 0.02	494	0.19 ± 0.01	2
NGC 6218	0.38 ± 0.03	343	1.48	0.35 ± 0.03	240	0.40 ± 0.03	2
NGC 6254	0.51 ± 0.02	624	1.64	0.53 ± 0.02	474	0.36 ± 0.03	1
NGC 6366	0.56 ± 0.05	105	0.93	0.49 ± 0.06	47	0.43 ± 0.05	1
NGC 6712	0.61 ± 0.03	304	1.28	0.57 ± 0.04	194	⋯	1
NGC 6752	0.33 ± 0.02	543	1.96	0.31 ± 0.02	452	0.29 ± 0.03	2
NGC 6809	0.24 ± 0.02	347	1.06	0.27 ± 0.03	187	0.31 ± 0.03	2
NGC 6838	0.66 ± 0.03	224	0.98	0.64 ± 0.05	106	0.62 ± 0.09	1
NGC 6934	0.26 ± 0.02	284	2.06	0.25 ± 0.03	264	0.30 ± 0.03	2
NGC 6981	0.49 ± 0.04	194	1.58	0.52 ± 0.04	144	0.56 ± 0.05	1
NGC 7006	0.52 ± 0.07	55	1.57	0.46 ± 0.09	46	⋯	1
NGC 7089	0.28 ± 0.02	451	2.52	0.25 ± 0.02	433	0.22 ± 0.02	2
NGC 7492	0.36 ± 0.04	117	0.99	0.36 ± 0.07	55	⋯	2

Notes. Values of the fraction of 1G stars with respect to the total number of analyzed stars and the number of analyzed stars outside the half-light radius are reported in the second, third, fifth, and sixth columns, which are obtained from the ground-based ChMs of the 29 GCs. The fourth column provides the ratio between the median radial distance of all the analyzed stars from the cluster center (R_{median}) and the cluster half-light radius (r_{hl}). The second-to-last column provides the fraction of 1G stars within the half-light radius, which is measured from the HST-based ChM. We indicate Group I and II in the last column.
[a] The fraction of 1G stars in the region outside the half-light radius.
[b] The fraction of 1G stars in the region inside the half-light radius.

a function of the median radius of the stars within each radial interval. We sorted these clusters according to metallicity, from the most metal-rich (NGC 5927, [Fe/H] = −0.49) to the most metal-poor (NGC 5053, [Fe/H] = −2.27). The relevant results are indicated with black circles, and the gray horizontal lines mark the extension of each radial interval determined to include the same number of stars. The 2G fraction of the entire sample of analyzed stars is marked with the aqua circle at their median radius. In Table 1, we provide this median radius of our entire sample for each cluster in units of half-light radius, R_{median}/r_{hl}, together with the corresponding fraction, to show in which region of the cluster the median radius of our entire samples is located. The magenta triangle indicates the literature results from A. P. Milone et al. (2017) based on the HST photometry, which is not indicated when the photometry is not available. The error associated with the 2G fraction has been determined by bootstrapping statistics. We generated random numbers as an equal size sample of the analyzed stars, then measured a ratio of the numbers smaller than the 2G fraction, and then this procedure was repeated 1000 times. The derived errors refer to one standard deviation of the bootstrapped measurement.

Corresponding to what is expected in most formation scenarios, in the majority of GCs the 2G fraction in the HST field of view is generally higher than that in the analyzed field of view of the ground-based photometry (see magenta and aqua circles in Figures 3 and 4). At the same time, we detected a large degree of variety in the 2G fraction as a function of the radial distance from the cluster center. Based on our results shown in Figures 3 and 4, we classified them into two groups according to the radial variation with its uncertainty. For metal-rich clusters ([Fe/H] $<$ −1.6, more metal-rich than NGC 7089) for which color separation between 1G and 2G in the ChM tends to be relatively clear, the classification also exploited the literature results by A. P. Milone et al. (2017). We identified the centrally concentrated 2G stars in NGC 5927, NGC 104, NGC 2808, NGC 1851, NGC 6981, NGC 5272, NGC 6254, NGC 3201, and NGC 6809, whereas stellar populations are spatially mixed in NGC 6366, NGC 6838, NGC 6712, NGC 6121, NGC 1261, NGC 5904, NGC 288, NGC 6218, NGC 6934, NGC 6205, NGC 6752, NGC 1904, NGC 7089, NGC 7492, NGC 4147, NGC 4833, NGC 2298, NGC 4590, and NGC 5053. NGC 7006, where we observe a larger fraction of 2G stars in the external region, is a possible exception. However, the smallest sample size restricts us from making a firm conclusion for this cluster.

E. Dondoglio et al. (2021) investigated stellar populations along the horizontal branch (HB) by means of the ground-based photometric diagram, V versus $C_{U,B,I}$, of four metal-rich Galactic GCs, NGC 104, NGC 5927, NGC 6366, and NGC 6838. They

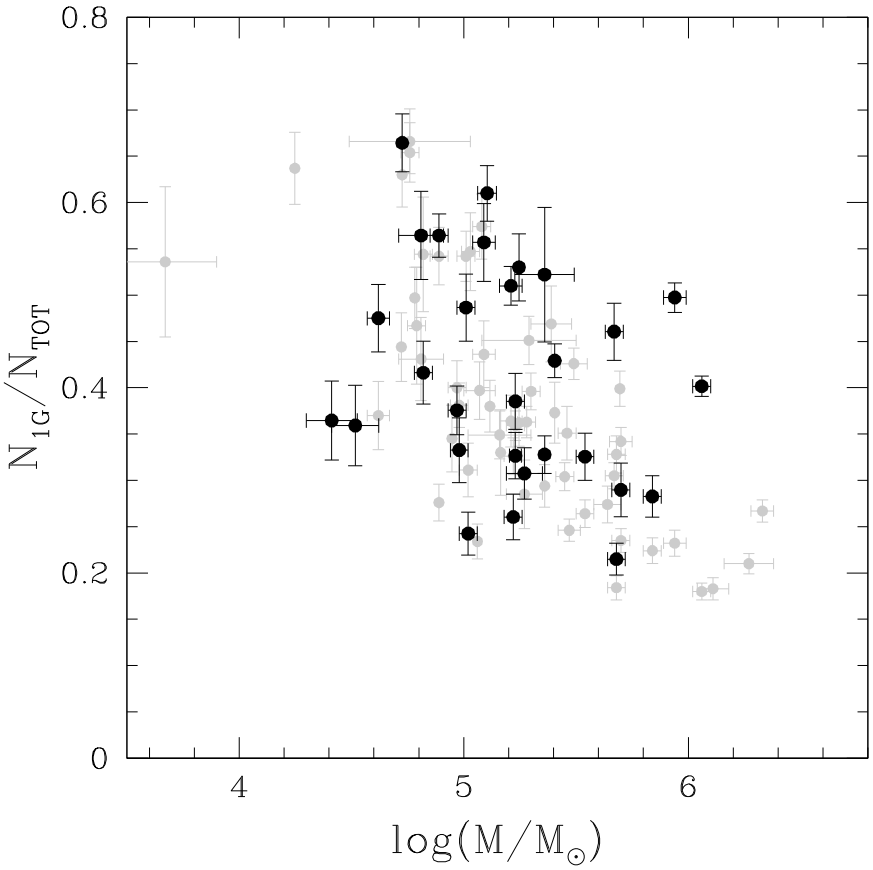

Figure 5. Fraction of 1G stars against the present-day cluster mass for Galactic GCs. Gray circles indicate literature results, which were derived from the HST-based ChMs (A. P. Milone et al. 2017; E. Dondoglio et al. 2021), whereas the fraction calculated from the ground-based ChMs are marked with black circles. Cluster masses are from H. Baumgardt & M. Hilker (2018).

derived the radial distribution of the 2G fraction from distinct sequences of 1G and 2G stars on the red HB, which can be detected in metal-rich GCs with [Fe/H] $\gtrsim$ −1.0 with appropriate photometric diagrams. Our finding is consistent with their conclusion that 2G stars in NGC 104 and NGC 5927 are more centrally concentrated than 1G stars, while the distribution is quite flat in NGC 6366 and NGC 6838.

E. Leitinger et al. (2023) performed wide-view analysis of multiple populations in 28 Galactic GCs by combining HST photometry with the wide-field ground-based photometry. For the 10 dynamically young GCs (age/relaxation time $<$ 4.5), for which they provided radial distributions of the fraction of 2G stars, we were able to compare their results with ours. We noticed that similar radial distributions to ours are found in NGC 288, NGC 2808, NGC 4590, NGC 5272, NGC 5904, NGC 6205, NGC 7089, NGC 6809, and NGC 5053. In contrast, they found that 1G stars in NGC 3201 are more centrally concentrated than 2G stars, at odds with our result of centrally concentrated 2G stars in this cluster.

Most previous studies qualitatively corroborated a 2G concentration in NGC 3201 (E. Carretta et al. 2010; V. Kravtsov et al. 2010; S. Lucatello et al. 2015; S. Kamann et al. 2020; V. Kravtsov & F. A. Calderón 2021), but recent studies on the radial configuration of stellar populations in NGC 3201 have presented somewhat-conflicting results. E. A. Hartmann et al. (2022) discovered a 1G central concentration by combining HST photometry with photometry from the S-PLUS survey, while V. J. Mehta et al. (2025) found more centrally concentrated 2G stars by introducing new photometric bands sensitive to the different chemical compositions of multiple populations from Gaia DR3 low-resolution XP spectra. Fuzzy separation of stellar populations in the photometric diagrams, along with potential incompleteness in the correction for severe differential reddening, could be one of the reasons for this discrepancy observed in NGC 3201. Improved photometric and spectroscopic data would be required to reach a consistent result on the radial distribution of stellar populations in NGC 3201.

4. The Fraction of 1G Stars and Global Cluster Parameters

In the following, we investigate the fraction of 1G stars in the analyzed field of view. As described in Section 2, the procedure to estimate the fraction with respect to the total number of stars ($N_{\rm TOT}$) is illustrated in the top panels of Figure 2 for NGC 2808. The resulting fractions of 1G stars are listed in Table 1, where we also provide the total number of RGB stars and the median radial distance of stars included in the $\Delta_{CU,B,I}$ versus $\Delta_{B,I}$ ChMs in units of half-light radius, as mentioned in Section 3. The fractions of 1G stars against the present-day cluster mass for Galactic GCs are plotted in Figure 5. It is immediately clear that the 1G fraction generally anticorrelates with cluster mass as already reported in the literature, but, at the same time, it is clearly bifurcated across all mass ranges.

As shown in the top left panel of Figure 6, we divided them into two groups of GCs based on the visually identifiable separation, Group I with higher 1G fraction and Group II with lower 1G fraction at a given mass. The Spearman's rank

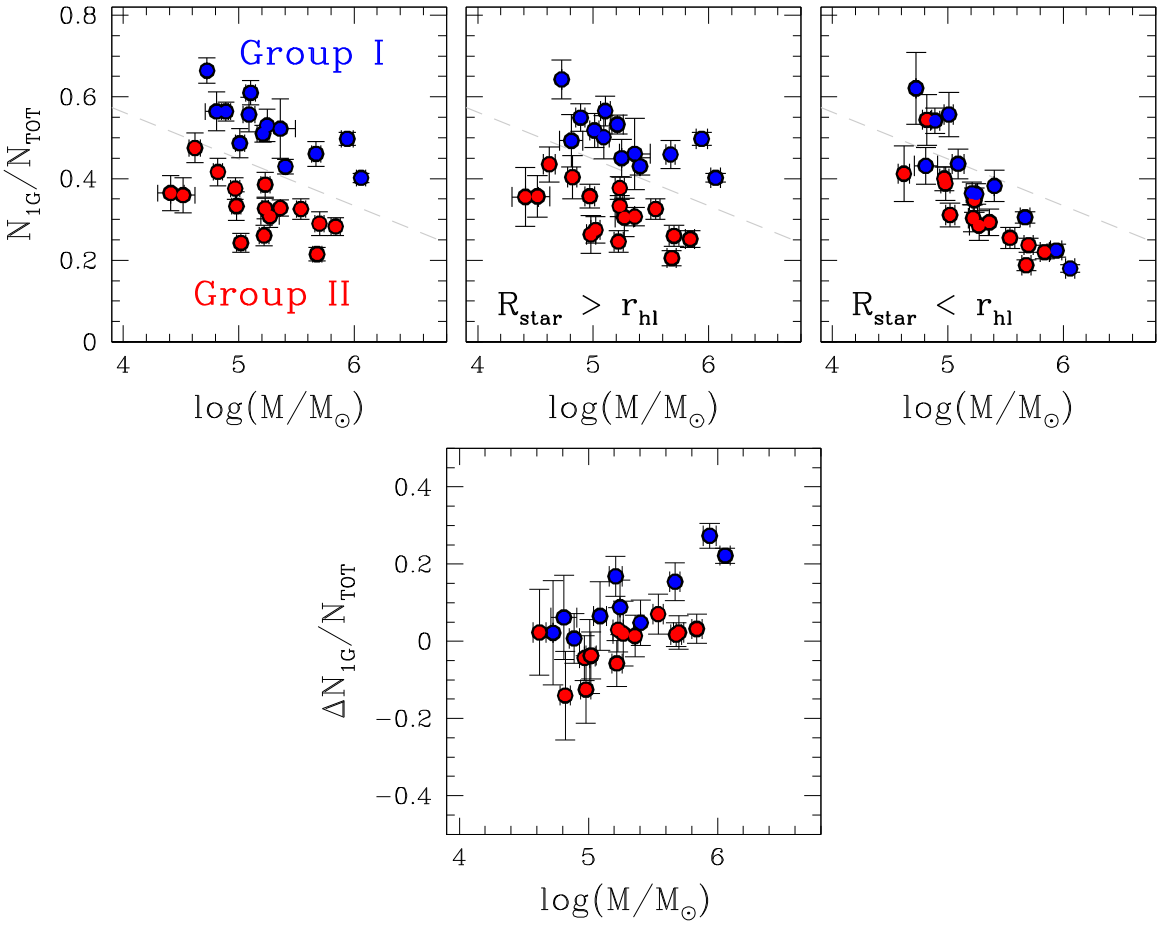

Figure 6. The top left panel is the same as Figure 5, but we divided the investigated targets into two groups, namely Group I (blue circles) and Group II (red circles). The top middle panel shows the 1G fraction in the region outside the half-light radius as a function of cluster mass. The top right panel illustrates the fraction of 1G stars inside the half-light radius, which is derived from the HST-based ChMs. The difference in the fractions of 1G stars inside and outside the half-light radius is plotted as a function of the cluster mass in the bottom panel.

correlation coefficient R_S for the relation between N_{1G}/N_{TOT} and the cluster mass is −0.32, −0.79, and −0.67 for the whole sample of GCs, Group I, and Group II, which are significant at p-value = 0.047, 0.001, and 0.002, respectively. Although we showed in Figure 1 that our sample of stars represents the region outside of the central region of clusters, in order to be more consistent in comparative studies among GCs, we also derived the fraction of 1G stars in the region outside the half-light radius, which is measured by excluding stars within the half-light radius. This fraction is also listed in Table 1 and is shown in the top middle panel of Figure 6. As expected, despite a larger uncertainty due to a smaller number of analyzed stars, the dichotomy still exists when removing stars within the half-light radius. For comparison, we also derived the fraction of 1G stars inside the half-light radius, as shown in the top right panel. This is measured by removing stars outside the half-light radius from the HST-based ChM (A. P. Milone et al. 2017). A small difference in the fractions between Group I and II clusters across cluster mass ranges is also detected, but the two groups are not separated on the diagram.

Results from the fractions of 1G stars inside and outside the half-light radii imply that clusters in Group II may have more efficiently lost their 1G stars in the outermost cluster regions, while Group I GCs have relatively retained the memory of the initial distribution of 1G and 2G stars. This is further supported by the fact that in Group I massive clusters have a significantly higher fraction of 1G stars outside the half-light radius compared to the fraction of 1G stars inside the half-light radius. The bottom panel illustrates the difference in the 1G fractions between the regions outside and inside the half-light radius, $\Delta N_{1G}/N_{TOT}$, which is obtained by subtracting the 1G fraction in the region inside the half-light radius from the fraction in the region outside the half-light radius. This difference implies the extent of central concentration of stellar populations, showing the correlation with cluster mass. However, clusters of Group II, which are expected to be relaxed and have their populations relatively mixed, have lower $\Delta N_{1G}/N_{TOT}$ than those of Group I.

4.1. Relation with the Radial Distribution of the Fraction of 2G Stars in GCs

Figure 7 is the same as the middle panel of Figure 6, but color-coded according to the trends of radial distribution classified in Section 3. We found that nearly all clusters of Group II have spatially mixed stellar populations. Two possible exceptions are NGC 1851 and NGC 6809 with centrally concentrated 2G stars. NGC 1851 is one of the peculiar GCs having additional stellar populations with enhancement in Fe and heavy elements. This population forms the additional sequence on the ChM, which is considered as 2G stars for simplicity when deriving the fraction of stellar populations (S. Jang et al. 2022). It therefore would become somewhat

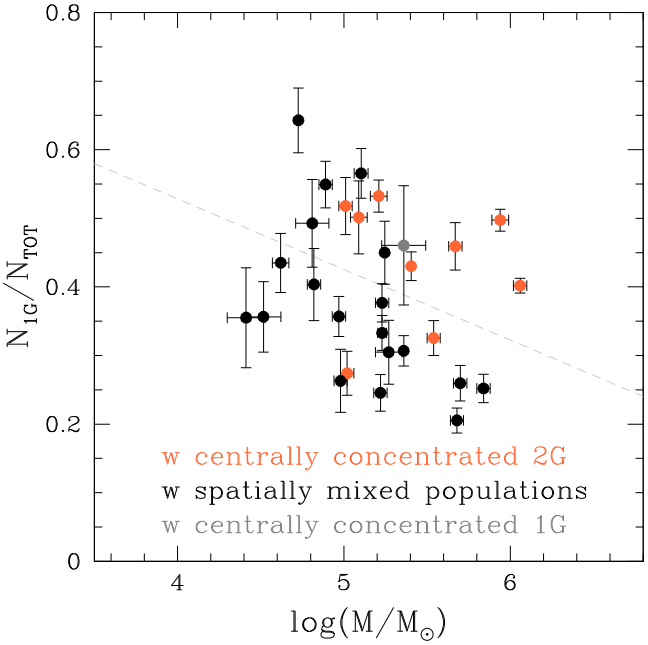

Figure 7. Same as the middle panel of Figure 6, but color-coded by classification by the trend of radial distribution. Black circles mark the clusters with spatially mixed stellar populations, while clusters with centrally concentrated 2G stars are colored in orange. Gray circles indicate NGC 7006 with centrally concentrated 1G stars.

difficult to directly compare the fraction of this cluster with those of other clusters. In spite of 2G stars being more centrally concentrated in NGC 6809, it is known for this cluster to have undergone a significant amount of mass loss of $M_{\rm current}/M_{\rm initial} = 0.261$ (H. Baumgardt et al. 2019; E. Leitinger et al. 2023), as predicted for Group II GCs. Thus, we could not clearly conclude that the centrally concentrated 2G stars in NGC 6809 reflect its initial spatial distribution of populations. Conversely, the radial distributions of 2G stars in Group I GCs are more complex. Massive GCs of Group I have more centrally concentrated 2G stars, while the radial distributions in less massive Group I GCs appear to be flat. This is hardly surprising, as less massive clusters tend to have shorter relaxation timescales (L. Spitzer 1987). It is expected that Group II GCs have undergone much dynamical mixing, all having spatially blended stellar populations, while relatively mild dynamic evolution has proceeded in Group I GCs, retaining their initial spatial condition, at least, in massive GCs.

As described above, E. Leitinger et al. (2023) combined HST photometry with the wide-field ground-based photometry to investigate the multiple-population phenomenon over a wide field of view. The sample of GCs investigated by E. Leitinger et al. (2023) comprises 21 clusters, which are also studied in this paper. While the radial distribution of each population intuitively illustrates the changes in the number fraction of each population as a function of radius, quantifying the difference in the radial distribution between 1G and 2G stars is rather challenging. In contrast, the cumulative radial distribution of the stars in each population, which E. Leitinger et al. (2023) primarily used, schematically displays the differences in the distribution of 1G and 2G stars within the cluster, and the difference can be quantified by the parameter A^+ introduced by E. Alessandrini et al. (2016). They quantified different radial profiles of 1G and 2G stars by using the area enclosed between their cumulative radial distributions, A^+, across the full extent of each cluster. This parameter indicates whether a cluster has centrally concentrated 2G stars ($A^+ < 0$), centrally concentrated 1G stars ($A^+ > 0$), or spatially mixed stellar populations ($A^+ \sim 0$). They investigated the resulting A^+ as a function of dynamical age, which is defined as the ratio of a cluster's age to its half-mass relaxation time, age$/t_{\rm rh}$. They found that dynamically old GCs (age$/t_{\rm rh} > 4.5$) all have $A^+ \sim 0$, while a wide range of A^+ is observed in dynamically young GCs (age$/t_{\rm rh} < 4.5$).

Figure 8 illustrates the fraction of 1G stars as a function of dynamical age. The fractions of 1G stars in Group I and Group II GCs appear to weakly to moderately correlate with dynamical age. The Spearman's rank correlation coefficients are $R_{\rm S} = 0.42$ with a p-value $= 0.074$ for Group I and $R_{\rm S} = 0.38$ with a p-value $= 0.074$ for Group II, showing slight but ultimately inconclusive correlations. In addition, we noticed that the 1G fractions, including the literature result represented by gray circles, of dynamically old GCs appear to exhibit relatively similar values. In contrast, dynamically young GCs display a wide range of 1G fractions. Considering the result of E. Leitinger et al. (2023) that dynamically old clusters all have fully mixed populations, this implies that such clusters have undergone significant dynamical mixing during their lifetime and lost their 1G stars preferentially in their outer regions, leading to similar 1G fractions. The right panel is the same as the left panel, but color-coded according to the categorized trend of radial distributions of the 2G fraction. We noticed that most dynamically old clusters (age$/t_{\rm rh} \gtrsim 10$) have spatially fully mixed stellar populations, whereas clusters with lower dynamical age (age$/t_{\rm rh} \lesssim 10$) have various spatial configurations of stellar populations, including not only centrally concentrated 2G but also spatially blended stellar populations. This result is qualitatively in agreement with previous findings by E. Leitinger et al. (2023).

4.2. Relation with Global Dynamical Properties

Here we investigate relations between the two groups of GCs and kinematic properties of the host GCs. Figure 9 shows the 1G fraction as a function of galactic radius, $R_{\rm GC}$, and perigalactic distance, $R_{\rm PER}$ (from H. Baumgardt & M. Hilker 2018), which reveals that the Group II GCs in red tend to have a wide range of $R_{\rm GC}$ and smaller perigalactic radii $R_{\rm PER} < 3.5$ kpc, except for most metal-poor GCs, NGC 4590, and NGC 5053 with the largest perigalactic radii. This is consistent with previous findings by M. Zennaro et al. (2019) and A. P. Milone et al. (2020) that GCs with large perigalactic distances ($R_{\rm PER} > 3.5$ kpc) tend to have a larger fraction of 1G stars than GCs with $R_{\rm PER} < 3.5$ kpc.

Recently, D. Massari et al. (2019) identified GCs with a common origin by analyzing the kinematic properties provided by Gaia data in the space of integral of motion (IOM), including the energy E and the angular momentum in the z-direction, L_z, which is perpendicular to the Galactic plane. We explored the link between our groups of GCs and the space of the IOM with probable progenitor galaxies of GCs provided by Massari and collaborators, together with the age–metallicity relation (AMR). Absolute ages and metallicity are from J. M. D. Kruijssen et al. (2019) and W. E. Harris (1996), respectively. The top and bottom panels of Figure 10 show the IOM and AMR for the clusters in our sample, respectively, color-coded according to the two groups of GCs and shape-

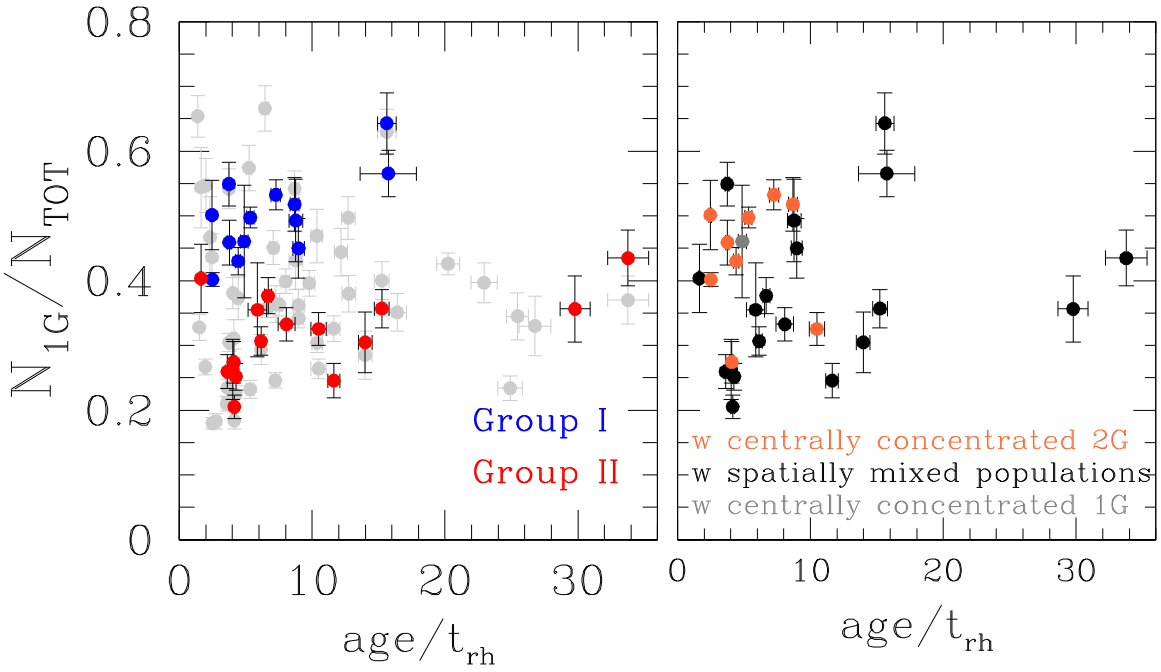

Figure 8. Fraction of 1G stars as a function of dynamical age, which is defined as the ratio of the cluster's age to its half-mass relaxation timescale. Gray circles plotted in the left panel represent literature results derived from the HST-based ChMs (A. P. Milone et al. 2017; E. Dondoglio et al. 2021). Ages and half-mass relaxation time, t_{rh}, are taken from J. M. D. Kruijssen et al. (2019) and H. Baumgardt (2017), respectively. Clusters are color-coded according to the group of GCs (left panel) and the categorized trend of radial distributions of the 2G fraction (right panel).

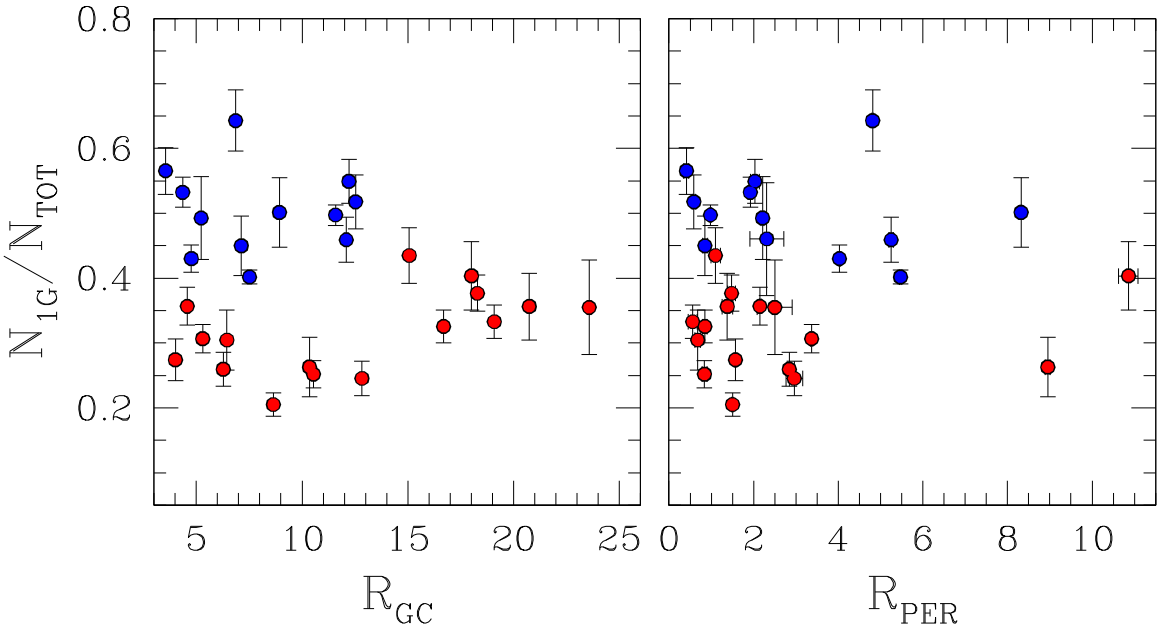

Figure 9. The fraction of 1G stars as a function of galactic and perigalactic radius. The Group I and Group II GCs defined in the N_{1G}/N_{TOT} and cluster mass plane are represented with blue and red circles, respectively.

coded by associations with different progenitors. The following is immediately clear:

1. *Clusters associated with Gaia–Enceladus (G-E) and Helmi stream (H99).* Among these GCs, clusters of Group II mostly have higher energy than those of Group I. The only exception is NGC 6205 with $E = -1.73 \times 10^5$ and $L_z = -251$. In 100,000 Monte Carlo simulations where we assumed that the simulated GCs have the same distribution as the observed clusters associated with G-E and H99 in the IOM, we find that the probability that 10 or 11 out of 11 randomly extracted GCs have energy more than -1.41×10^5 is 0.013. In addition, the AMR of Group II appears to be slightly shifted by $\sim$0.2 dex toward the metal-poor side from the AMR of Group I GCs, but we could not confidently conclude this owing to large errors of cluster age.
2. *Clusters associated with main progenitor (MP).* Due to the small sample of GCs associated with the MP, it would be difficult to argue that there is a clear difference in

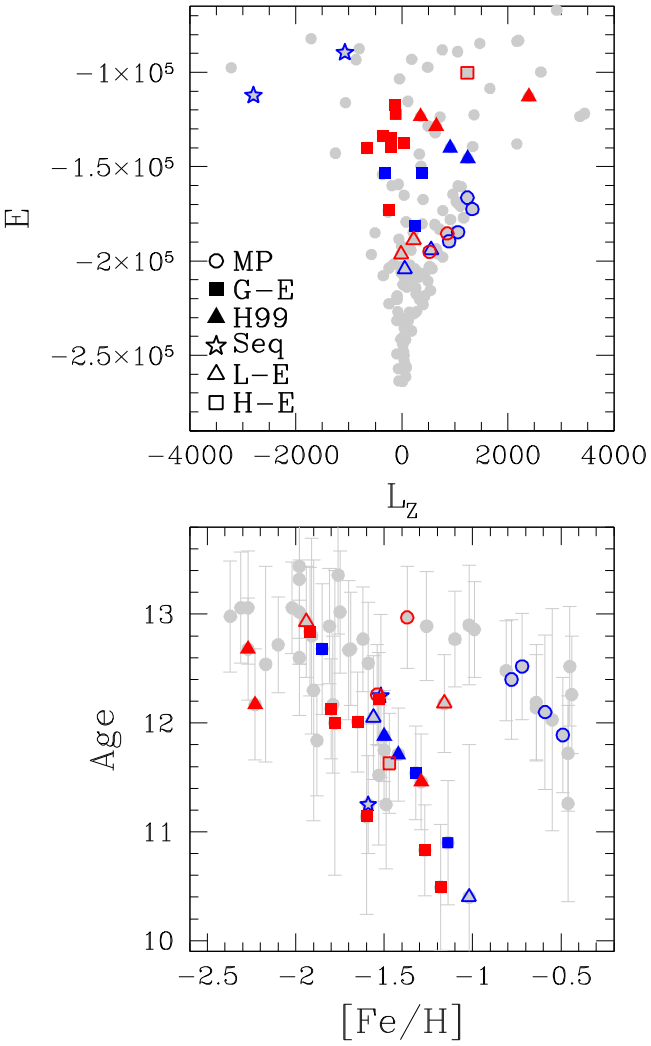

Figure 10. Top panel: E vs. L_z projections of the IOM space for 151 GCs (from D. Massari et al. 2019). Group I and Group II GCs are colored in blue and red, respectively, shape-coded according to their associations with different progenitors (open circles mark the MP, filled squares are for G-E, filled triangles are for H99, stars are for Sequoia, open triangles are for the low-energy group, and open squares are for the high-energy group). Bottom panel: AMR for Galactic GCs. Ages and metallicity are taken from J. M. D. Kruijssen et al. (2019) and the 2010 version of the W. E. Harris (1996) catalog. Clusters are color- and shape-coded in the same way as in the top panel.

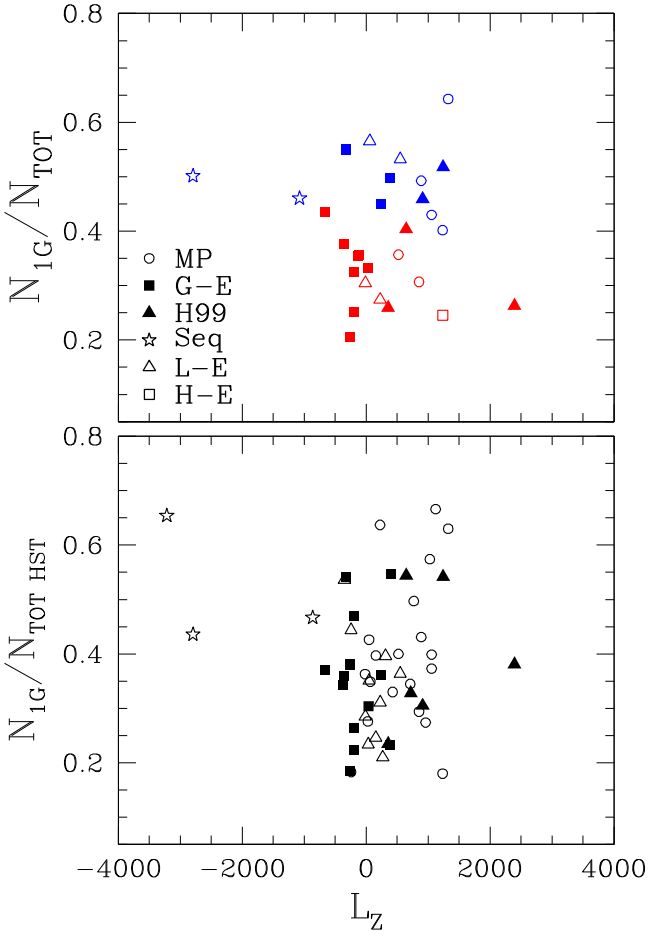

Figure 11. N_{1G}/N_{TOT} vs. L_z for Galactic GCs. N_{1G}/N_{TOT} in the top and bottom panels mark the results derived from ground-based and HST photometry, respectively. Group I and Group II GCs are colored in blue and red in the top panel, respectively. Clusters are shape-coded as shown in Figure 10 according to associations with different progenitors.

energy and L_z between the two groups of GCs. We noticed, however, that Group II GCs, NGC 6218, and NGC 6752 are definitely more metal-poor than Group I GCs as shown in the AMR.

3. *Clusters associated with Sequoia (Seq).* Two clusters associated with Sequoia in our sample of GCs, NGC 3201 and NGC 7006, have retrograde orbits and very high energies. Unlike other GCs with high energy, these two GCs belong to Group I.

For GCs associated with low energy (L-E), no relations between the two groups of GCs and the IOM space are found, but Group II GCs seem to be older than Group I GCs. In fact, D. Massari et al. (2019) labeled some GCs, which were not able to be associated with known merger events, L-E or H-E according to their energy level. Hence, they cannot have a common origin.

The top and bottom panels of Figure 11 show L_z versus N_{1G}/N_{TOT} from this study and A. P. Milone et al. (2017), respectively. We found that the fraction of 1G stars appears to mildly anticorrelate with L_z in both groups. This is indicated by the Spearman's rank correlation coefficients, which are R_S = –0.10 for Group I and –0.23 for Group II. On the contrary, no correlation is found between L_z and the 1G fractions in the HST field of view.

5. Summary and Conclusions

In this work, we have analyzed the $\Delta c_{U,B,I}$ versus $\Delta_{B,I}$ pseudo–two-color diagrams of RGB stars for 29 GCs from S. Jang et al. (2022; see their Figures 12 and 13) to investigate multiple stellar populations over a wide field of view. The ChMs allowed us to derive the fractions of stellar populations in the wide-field spatial extent of a large sample of GCs, which have various implications for interplay between the multiple populations and the galactic environment. In particular, we explored whether the fraction of stellar populations in the analyzed field of view has been influenced by GC global parameters and the dynamic evolution of GCs in our Galaxy. The main results can be summarized as follows:

1. We classified the analyzed GCs into two groups based on the radial distribution of 2G stars: GCs with centrally concentrated 2G stars and GCs with spatially mixed populations. The former include NGC 5927, NGC 104, NGC 2808, NGC 1851, NGC 6981, NGC 5272, NGC 6254, NGC 3201, and NGC 6809. The latter include NGC 6366, NGC 6838, NGC 6712, NGC 6121, NGC 1261, NGC 5904, NGC 288, NGC 6218, NGC 6934, NGC 6205, NGC 6752, NGC 1904, NGC 7089, NGC 7492, NGC 4147, NGC 4833, NGC 2298, NGC 4590, and NGC 5053. NGC 7006 with a larger fraction of 2G stars in the external region is a possible exception. However, small statistics prevent us from a firm conclusion for this cluster. Thus, we conclude that all the GCs either have a flat distribution or exhibit more centrally concentrated 2G stars.
2. The resulting fractions of 1G stars in the analyzed field of view generally anticorrelate with cluster mass as already discovered in the literature, but, at the same time, they are clearly bifurcated across all mass ranges, allowing us to divide them into two groups of GCs. We referred to groups of clusters with higher and lower fractions as Group I and Group II, respectively.
3. The dichotomy still exists when removing stars within the half-light radius, implying that a group of GCs with lower 1G fractions at given masses of clusters might have more efficiently lost their 1G stars in the outermost cluster regions.
4. We studied the link between the two groups of GCs and the categorized radial distributions of the 2G fraction. We find that almost all GCs in Group II exhibit flat radial distributions of 2G stars, while the distributions tend to be flat in only less massive GCs among Group I GCs. Massive GCs in Group I have more centrally concentrated 2G stars.
5. Group II GCs span a wider range of R_{GC} and have smaller perigalactic radii $R_{PER} < 3.5$ kpc, except for the most metal-poor GCs, NGC 4590, and NGC 5053 with the largest perigalactic radii.
6. We used the IOM space and probable progenitor galaxies of GCs provided by D. Massari et al. (2019), including AMR, to explore the link between those and the two groups of GCs defined in this work. We find that Group II GCs tend to have higher energy and to be relatively metal-poor, especially in the case of clusters associated with G-E and H99. Among clusters formed in situ referred to as the MP, Group II GCs are more metal-poor than Group I GCs.
7. The fraction of 1G stars inferred from wide-field photometry appears to mildly anticorrelate with the z-angular momentum L_z of GCs toward the Galactic north pole in both groups of GCs. No correlation is found with the 1G fractions in the central region derived from the HST photometry.

The analysis of wide-field ground-based ChMs of RGB stars in 29 GCs provides observational evidence of the dynamic path that GCs and stellar populations in them have stepped on. Our study is the first to have shown a clear dichotomy of GCs in the number ratio of the first population to the total number of stars analyzed at given masses of GCs. A link between the kinematic information of GCs and the two groups of GCs identified in this study implies that Group II GCs have experienced more drastic dynamic evolution, losing more stars in the outermost cluster region. Although additional work is needed to constrain the initial physical properties of clusters and the kinematic paths they have followed in the context of different assembly history, our result provides a global view of the dynamical evolution of Galactic GCs.

Acknowledgments

This research was supported by Basic Science Research Program through the National Research Foundation of Korea (NRF) funded by the Ministry of Education (RS-2022-NR070872) and by the NRF grant funded by the Korea government (MSIT) (RS-2022-NR070525). A.P.M., G.C., and A.F.M. acknowledge the support received from the European Union's Horizon 2020 research and innovation program under the Marie Skłodowska-Curie grant agreement No. 101034319 and from INAF Research GTO-grant Normal RSN 2-1.05.12.05.10—Understanding the formation of globular clusters with their multiple stellar generations (ref. A.F.M.) of the "Bando INAF per il Finanziamento della Ricerca Fondamentale 2022." E.P.L. acknowledges support from the "Science & Technology Champion Project" (202005AB160002) and from the "Top Team Project" (202305AT350002), all funded by the "Yunnan Revitalization Talent Support Program."

ORCID iDs

S. Jang https://orcid.org/0000-0002-1562-7557
A. P. Milone https://orcid.org/0000-0001-7506-930X
A. F. Marino https://orcid.org/0000-0002-1276-5487
M. Tailo https://orcid.org/0000-0002-1128-098X
E. Dondoglio https://orcid.org/0000-0001-8415-8531
M. V. Legnardi https://orcid.org/0000-0003-3153-1499
G. Cordoni https://orcid.org/0000-0002-7690-7683
T. Ziliotto https://orcid.org/0000-0001-8538-2068
E. P. Lagioia https://orcid.org/0000-0003-1713-0082
M. Carlos https://orcid.org/0000-0003-1757-6666
A. Mohandasan https://orcid.org/0000-0001-5182-0330
Y.-W. Lee https://orcid.org/0000-0002-2210-1238

References

Alessandrini, E., Lanzoni, B., Ferraro, F. R., Miocchi, P., & Vesperini, E. 2016, ApJ, 833, 252
Bastian, N., Kamann, S., Cabrera-Ziri, I., et al. 2018, MNRAS, 480, 3739
Bastian, N., Lamers, H. J. G. L. M., de Mink, S. E., et al. 2013, MNRAS, 436, 2398
Baumgardt, H. 2017, MNRAS, 464, 2174
Baumgardt, H., & Hilker, M. 2018, MNRAS, 478, 1520
Baumgardt, H., Hilker, M., Sollima, A., & Bellini, A. 2019, MNRAS, 482, 5138
Carretta, E., Bragaglia, A., D'Orazi, V., Lucatello, S., & Gratton, R. G. 2010, A&A, 519, A71
Carretta, E., Bragaglia, A., Gratton, R. G., et al. 2009, A&A, 505, 117
Conroy, C. 2012, ApJ, 758, 21
Cordoni, G., Casagrande, L., Milone, A., et al. 2025, MNRAS, 537, 2342
Cordoni, G., Marino, A. F., Milone, A. P., et al. 2023, A&A, 678, A155
Cordoni, G., Milone, A. P., Marino, A. F., et al. 2020, ApJ, 898, 147
Cordoni, G., Milone, A. P., Marino, A. F., et al. 2022, NatCo, 13, 4325
Dalessandro, E., Cadelano, M., Vesperini, E., et al. 2019, ApJL, 884, L24
D'Antona, F., Vesperini, E., D'Ercole, A., et al. 2016, MNRAS, 458, 2122
Decressin, T., Meynet, G., Charbonnel, C., Prantzos, N., & Ekström, S. 2007, A&A, 464, 1029
de Mink, S. E., Pols, O. R., Langer, N., & Izzard, R. G. 2009, A&A, 507, L1
Denissenkov, P. A., & Hartwick, F. D. A. 2014, MNRAS, 437, L21
D'Ercole, A., Vesperini, E., D'Antona, F., McMillan, S. L. W., & Recchi, S. 2008, MNRAS, 391, 825
Dondoglio, E., Milone, A. P., Lagioia, E. P., et al. 2021, ApJ, 906, 76
Dondoglio, E., Milone, A. P., Marino, A. F., et al. 2023, MNRAS, 526, 2960
Gaia Collaboration, Brown, A. G. A., Vallenari, A., et al. 2018, A&A, 616, A1

Gaia Collaboration, Brown, A. G. A., Vallenari, A., et al. 2021, A&A, 649, A1
Gieles, M., Charbonnel, C., Krause, M. G. H., et al. 2018, MNRAS, 478, 2461
Gratton, R., Bragaglia, A., Carretta, E., et al. 2019, A&ARv, 27, 8
Gratton, R., Sneden, C., & Carretta, E. 2004, ARA&A, 42, 385
Grundahl, F., VandenBerg, D. A., & Andersen, M. I. 1998, ApJL, 500, L179
Harris, W. E. 1996, AJ, 112, 1487
Hartmann, E. A., Bonatto, C. J., Chies-Santos, A. L., et al. 2022, MNRAS, 515, 4191
Jang, S., & Lee, Y.-W. 2015, ApJS, 218, 31
Jang, S., Lee, Y. W., Joo, S. J., & Na, C. 2014, MNRAS, 443, L15
Jang, S., Milone, A. P., Lagioia, E. P., et al. 2021, ApJ, 920, 129
Jang, S., Milone, A. P., Legnardi, M. V., et al. 2022, MNRAS, 517, 5687
Kamann, S., Giesers, B., Bastian, N., et al. 2020, A&A, 635, A65
Kim, J. J., & Lee, Y.-W. 2018, ApJ, 869, 35
Kravtsov, V., Alcaíno, G., Marconi, G., & Alvarado, F. 2010, A&A, 512, L6
Kravtsov, V., & Calderón, F. A. 2021, AJ, 161, 7
Kruijssen, J. M. D., Pfeffer, J. L., Reina-Campos, M., Crain, R. A., & Bastian, N. 2019, MNRAS, 486, 3180
Lagioia, E. P., Milone, A. P., Legnardi, M. V., et al. 2025, ApJ, 979, 30
Lagioia, E. P., Milone, A. P., Marino, A. F., & Dotter, A. 2019, ApJ, 871, 140
Lee, J.-W. 2017, ApJ, 844, 77
Lee, Y.-W., & Jang, S. 2016, ApJ, 833, 236
Lee, Y. W., Joo, J. M., Sohn, Y. J., et al. 1999, Natur, 402, 55
Lee, Y.-W., Joo, S.-J., & Chung, C. 2015, MNRAS, 453, 3906
Lee, Y.-W., Joo, S.-J., Han, S.-I., et al. 2005, ApJL, 621, L57
Legnardi, M. V., Milone, A. P., Armillotta, L., et al. 2022, MNRAS, 513, 735
Legnardi, M. V., Milone, A. P., Cordoni, G., et al. 2023, MNRAS, 522, 367
Leitinger, E., Baumgardt, H., Cabrera-Ziri, I., Hilker, M., & Pancino, E. 2023, MNRAS, 520, 1456
Libralato, M., Vesperini, E., Bellini, A., et al. 2023, ApJ, 944, 58
Lucatello, S., Sollima, A., Gratton, R., et al. 2015, A&A, 584, A52
Marino, A. F., Milone, A. P., Legnardi, M. V., et al. 2024, ApJ, 965, 189
Marino, A. F., Villanova, S., Piotto, G., et al. 2008, A&A, 490, 625
Massari, D., Koppelman, H. H., & Helmi, A. 2019, A&A, 630, L4
Mehta, V. J., Milone, A. P., Casagrande, L., et al. 2025, MNRAS, 536, 1077
Milone, A. P., Cordoni, G., Marino, A. F., et al. 2023a, A&A, 672, A161
Milone, A. P., & Marino, A. F. 2022, Univ, 8, 359
Milone, A. P., Marino, A. F., Da Costa, G. S., et al. 2020, MNRAS, 491, 515
Milone, A. P., Marino, A. F., Dotter, A., et al. 2023b, MNRAS, 522, 2429
Milone, A. P., Piotto, G., Bedin, L. R., et al. 2012a, ApJ, 744, 58
Milone, A. P., Piotto, G., Bedin, L. R., et al. 2012b, A&A, 540, A16
Milone, A. P., Piotto, G., King, I. R., et al. 2010, ApJ, 709, 1183
Milone, A. P., Piotto, G., Renzini, A., et al. 2017, MNRAS, 464, 3636
Mohandasan, A., Milone, A. P., Cordoni, G., et al. 2024, A&A, 681, A42
Monelli, M., Milone, A. P., Stetson, P. B., et al. 2013, MNRAS, 431, 2126
Niederhofer, F., Bastian, N., Kozhurina-Platais, V., et al. 2017, MNRAS, 465, 4159
Piotto, G., Milone, A. P., Bedin, L. R., et al. 2015, AJ, 149, 91
Renzini, A., D'Antona, F., Cassisi, S., et al. 2015, MNRAS, 454, 4197
Renzini, A., Marino, A. F., & Milone, A. P. 2022, MNRAS, 513, 2111
Spitzer, L. 1987, Dynamical Evolution of Globular Clusters (Princeton, NJ: Princeton Univ. Press)
Stetson, P. B., Pancino, E., Zocchi, A., Sanna, N., & Monelli, M. 2019, MNRAS, 485, 3042
Vesperini, E., McMillan, S. L. W., D'Antona, F., & D'Ercole, A. 2013, MNRAS, 429, 1913
Wang, L., Kroupa, P., Takahashi, K., & Jerabkova, T. 2020, MNRAS, 491, 440
Yong, D., & Grundahl, F. 2008, ApJL, 672, L29
Zennaro, M., Milone, A. P., Marino, A. F., et al. 2019, MNRAS, 487, 3239